A dual role for planar cell polarity genes in ciliated cells

Camille Boutin[a], Paul Labedan[b], Jordane Dimidschstein[c], Fabrice Richard[d], Harold Cremer[d], Philipp André[e], Yingzi Yang[e], Mireille Montcouquiol[f], Andre M. Goffinet[a], and Fadel Tissir[a,1]

[a]Institute of Neuroscience, Developmental Neurobiology, Université catholique de Louvain, B1200 Brussels, Belgium; [b]PLab, B1200 Brussels, Belgium; [c]Institut de Recherches en Biologie Humaine et Moléculaire, Université Libre de Bruxelles, 1070 Brussels, Belgium; [d]Aix-Marseille Université, Centre National de la Recherche Scientifique, Institut de Biologie du Développement de Marseille Luminy, Unité Mixte de Recherche 7288, 13288 Marseille, France; [e]Developmental Genetics Section, Genetic Disease Research Branch, National Human Genome Research Institute, Bethesda, MD 20892; and [f]Planar Polarity and Plasticity Group, Institut National de la Santé et de la Recherche Médicale U862, Neurocenter Magendie, 33077 Bordeaux, France

Edited by Jeremy Nathans, Johns Hopkins University, Baltimore, MD, and approved June 24, 2014 (received for review March 18, 2014)

In the nervous system, cilia dysfunction perturbs the circulation of the cerebrospinal fluid, thus affecting neurogenesis and brain homeostasis. A role for planar cell polarity (PCP) signaling in the orientation of cilia (rotational polarity) and ciliogenesis is established. However, whether and how PCP regulates cilia positioning in the apical domain (translational polarity) in radial progenitors and ependymal cells remain unclear. By analysis of a large panel of mutant mice, we show that two PCP signals are operating in ciliated cells. The first signal, controlled by cadherin, EGF-like, laminin G-like, seven-pass, G-type receptor (Celsr) 2, *Celsr3*, *Frizzled3* (*Fzd3*) and *Van Gogh like2* (*Vangl2*) organizes multicilia in individual cells (single-cell polarity), whereas the second signal, governed by *Celsr1*, *Fzd3*, and *Vangl2*, coordinates polarity between cells in both radial progenitors and ependymal cells (tissue polarity). Loss of either of these signals is associated with specific defects in the cytoskeleton. Our data reveal unreported functions of PCP and provide an integrated view of planar polarization of the brain ciliated cells.

Epithelial ciliated cells have important functions, such as clearing mucus and debris in airways, assisting the transit of eggs in the oviduct, or facilitating circulation of the cerebrospinal fluid (CSF) in cerebral ventricles. The importance of ciliated cells is reflected by the variety of disorders that result from abnormal cilia assembly, motility, or polarity and lead, among others, to infertility, situs inversus, or hydrocephalus (1, 2). To fulfill their function, motile cilia must coordinate their beats in individual cells as well as across the whole tissue. In the brain, ependymal cells lining cerebral ventricles bear at their apical surface multiple cilia that beat in a concerted manner (3–5). During ependymal differentiation, cilia first appear randomly oriented (6). They subsequently rotate and adopt a common orientation, a process termed rotational polarity (6, 7). This polarity is coordinated between adjacent cells with cilia that point to a common direction. In addition, cilia basal bodies (BBs), which are initially widely scattered at the apical surface, cluster into an off-centered patch at one side of the apical domain, a feature referred to as translational polarity (7). A similar polarity is observed in radial glia (RG) cells from which ependymal cells differentiate perinatally (8). RG cells have a single primary cilium that is shifted from the cell center. The coordination of this displacement between neighboring cells is the first sign of tissue polarity (7).

Planar cell polarity (PCP) signaling was initially described in *Drosophila*, where it governs the stereotypic arrangement of wing hairs, bristles, and ommatidia through a set of core PCP genes (9–12). In mammals, PCP-dependent processes include neural tube closure, fur patterning, hair bundle orientation in the inner ear, neuronal migration, and axon guidance (13, 14). Mammalian core PCP genes include cadherin, EGF-like, laminin G-like, seven-pass, G-type receptor (Celsr) 1-3, *Frizzled3* (*Fzd3*), *Fzd6*, *Van Gogh like1-2* (*Vangl1-2*), *Disheveled1-3* (*Dvl1-3*), and *Prickle-like 1–4*. *Celsr2-3*, *Vangl2*, and *Dvl2* are implicated in cilia development and function. Their mutations affect the apical docking and rotational polarity of cilia in ependymal cells, leading to impaired flow circulation (5, 6, 15).

Despite recent advances, our understanding of PCP in RG and ependymal cells is still incomplete. Key questions remain. (*i*) Does PCP play a role in RG progenitors? (*ii*) Is PCP involved in translational polarity? (*iii*) How does the primary cilium in RG affect polarity of multicilia in mature cells? Here, we used a panel of PCP mutant mice as well as newly designed quantitative tools to scrutinize the role of PCP in radial progenitors and ependymal cells. We found that two PCP signals, which may be sorted by distinct *Celsr*s, act concomitantly to regulate different aspects of polarity. *Celsr1*, *Fzd3*, and *Vangl2* coordinate the positioning of the primary cilium in RG cells and harmonize the orientation and direction of displacement of ciliary patches across the ependyma (tissue polarity). *Celsr2*, *Celsr3*, *Fzd3*, and *Vangl2* organize cilia in individual cells (single-cell polarity).

Results

***Celsr1*, *Fzd3*, and *Vangl2* Coordinate Translational Polarity in Radial Progenitors.** RG cells that line embryonic and early postnatal lateral ventricles bear a primary cilium at their apical surface. We studied translational polarity of this cilium at embryonic day (E) 14.5 and postnatal day (P) 1 in four regions of the ventricular lateral wall (LW) (Fig. S1*A*). Consistent with reported data (7) the BB of the primary cilium was displaced from the center of the apical surface (mean displacement: 0.39 ± 0.14 at E14.5 and

Significance

Ependymal cilia are required for circulation of the cerebrospinal fluid and neurogenesis. To function properly, ependymal cilia must coordinate their beats in individual cells and across the tissue. Planar cell polarity (PCP) orients cilia in a given cell, thereby enabling their concerted beating. Here, we describe previously unidentified functions for PCP in cilia organization at the cell and tissue levels. We show that PCP is important for the correct positioning of the primary cilium in radial progenitors and motile cilia in ependymal cells and provide evidence that cilia positioning is important for function. We also describe cytoskeletal changes during ependymal differentiation and shed light on mechanisms by which polarity is acquired by radial progenitors and passed on to ependymal cells.

Author contributions: C.B., A.M.G., and F.T. designed research; C.B. and J.D. performed research; P.L., F.R., H.C., P.A., Y.Y., and M.M. contributed new reagents/analytic tools; C.B., A.M.G., and F.T. analyzed data; and C.B. and F.T. wrote the paper.

The authors declare no conflict of interest.

This article is a PNAS Direct Submission.

[1]To whom correspondence should be addressed. Email: fadel.tissir@uclouvain.be.

This article contains supporting information online at www.pnas.org/lookup/suppl/doi:10.1073/pnas.1404988111/-/DCSupplemental.

0.44 ± 0.18 at P1). However, whereas vectors of displacement were divergent at E14.5, they locally pointed to a common direction at P1, indicating that RG cells acquire their polarity during the perinatal period (Fig. S1 *B–K*) (7). We analyzed the mean vector of displacement and found that it constantly coincided with the functional axis (i.e., direction of CSF circulation) (Fig. S1 *A* and *G′–J′*). Given the robust expression of PCP genes in the periventricular region (16–20), we wondered whether they control translational polarity in RG cells and tested this using the following mutants: *Celsr1*$^{-/-}$ (21), *Celsr2*$^{-/-}$ (Fig. S2), *Celsr3*$^{-/-}$ (22), and *Fzd3*$^{-/-}$ (23). Because all *Vangl2*$^{-/-}$ mice have an open neural tube (24), we produced forebrain conditional mutants (*Vangl2*^{cKO}) by crossing *Vangl2* floxed (*f*) with *Foxg1-Cre* mice (25). We focused on the dorsoanterior aspect of the LW (Fig. 1*F*). Like control cells (WT), all PCP mutant RG cells had an off-centered primary cilium (Fig. 1 and Fig. S3). We measured the relative distance between the geometric center of the apical surface and the BB and observed no differences between WT and PCP mutants (WT = 0.41 ± 0.02; *Celsr1*$^{-/-}$ = 0.42 ± 0.03, P = 0.4101; *Celsr2*$^{-/-}$ = 0.43 ± 0.02, P = 0.1467; *Celsr3*$^{-/-}$ = 0.44 ± 0.02, P = 0.0794; *Fzd3*$^{-/-}$ = 0.40 ± 0.04, P = 0.6857; *Vangl2*^{cKO} = 0.43 ± 0.02, P = 0.2618) (Fig. 1 and Fig. S4), indicating that PCP is not involved in translational polarity at the single-cell level. We then analyzed the coordination of BB displacement at the tissue level by drawing a vector (VD) from the cell center to the BB (Fig. S5 *A* and *B*). Vectors from neighboring cells pointed roughly to a common direction in WT (Fig. 1 *A* and *C*), *Celsr2*$^{-/-}$, and *Celsr3*$^{-/-}$ LW (Fig. S4 *A–B′*). In contrast, they were more divergent in *Celsr1*$^{-/-}$ (Fig. 1 *B* and *D*), *Fzd3*$^{-/-}$, and *Vangl2*^{cKO} (Fig. S4 *C–D′*). Analysis with circular statistics showed that the angular deviation of individual vectors from the mean was comprised between −45° and +45° in WT, *Celsr2*$^{-/-}$, and *Celsr3*$^{-/-}$ but displayed broader distributions in *Celsr1*$^{-/-}$, *Fzd3*$^{-/-}$, and *Vangl2*^{cKO} mutant samples (Fig. 1*E*). These results show that PCP is dispensable for off-centering of BBs but coordinates the direction of their displacement through *Celsr1*, *Fzd3*, and *Vangl2*.

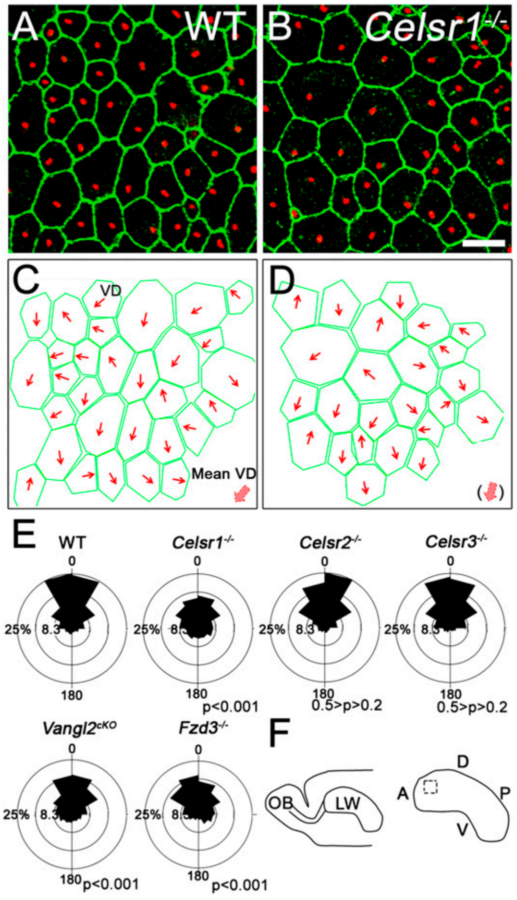

Fig. 1. Planar polarity in radial progenitors. (*A* and *B*) *En face* view of LW in (*A*) WT and (*B*) *Celsr1*$^{-/-}$ P1 mice stained for ZO1 (green) and γ-tubulin (red). (*C* and *D*) Trace of the cell contour (green). Red arrows, vectors of BB displacement (VD); thick red arrows, mean vector of displacement. Relative displacement calculated as the ratio of the distance between the center of the apical surface and the BB divided by the distance between the cell center and the membrane: WT = 0.41 ± 0.02; *Celsr1*$^{-/-}$ = 0.42 ± 0.03, P = 0.4101; *Celsr2*$^{-/-}$ = 0.43 ± 0.02, P = 0.1467; *Celsr3*$^{-/-}$ = 0.44 ± 0.02, P = 0.0794; *Fzd3*$^{-/-}$ = 0.40 ± 0.04, P = 0.6857; *Vangl2*^{cKO} = 0.43 ± 0.02, P = 0.2618. (*E*) Angular distribution of vectors of BB displacement around the mean. In WT, the majority of vectors are distributed between −45° and 45°, reflecting the coordination of primary cilium displacement. In the absence of functional Celsr1, Vangl2, or Fzd3, this coordination is lost, leading to a broader distribution. Note that inactivation of Celsr2 or Celsr3 does not affect this coordination (n = 1,075 cells in WT, 1,258 cells in *Celsr1*$^{-/-}$, 1,057 cells in *Celsr2*$^{-/-}$, 1,171 cells in *Celsr3*$^{-/-}$, 1,421 cells in *Vangl2*^{cKO}, and 1,167 cells in *Fzd3*$^{-/-}$; five animals for each genotype; Watson U^2 compared with WT: *Celsr1*$^{-/-}$ = 3.592, $P < 0.001$; *Celsr2*$^{-/-}$ = 0.082, $0.5 > P > 0.2$; *Celsr3*^{cKO} = 0.108, $0.5 > P > 0.2$; *Vangl2*^{cKO} = 1.576, $P < 0.001$; *Fzd3*$^{-/-}$ = 1.378, $P < 0.001$). (*F*) Schema of the lateral ventricular wall. Boxed area is the region of interest. A, anterior; D, dorsal; OB, olfactory bulb; P, posterior; V, ventral. (Scale bar: 10 μm.)

***Celsr2*, *Celsr3*, *Fzd3*, and *Vangl2* Organize Multicilia in Individual Cells.** We studied the formation of cilia patches in *Celsr1*$^{-/-}$, *Celsr2*$^{-/-}$, *Celsr3*$^{f/-}$;*Foxg1-Cre* (*Celsr3*^{cKO}), *Fzd3*$^{f/-}$;*Foxg1-Cre* (*Fzd3*^{cKO}), and *Vangl2*$^{f/-}$;*Foxg1-Cre* (*Vangl2*^{cKO}) mice. At P21, both WT and PCP mutant cells were garnished with multicilia. Their BBs were clustered in patches that covered about 20% of the apical domain in all genotypes. However, whereas patches were rounded in WT and *Celsr1*$^{-/-}$, many were irregular in *Celsr3*^{cKO}, *Fzd3*^{cKO}, and *Vangl2*^{cKO} and abnormally elongated in *Celsr2*$^{-/-}$ samples (Fig. 2 *A–F*). To estimate the patch shape variation, we calculated the length-to-width ratio and found it lower than two in control cells. Although there was a trend toward higher ratios in all mutant cells, the most significant shift was found in *Celsr2*$^{-/-}$ cells (Fig. 2*G*). Importantly, like in WT cells, BB patches were displaced from the apical geometric center in all PCP mutants (Fig. 2 *A–F*). We evaluated patch displacement by measuring the relative distance between the center of the apical surface and that of the patch and found no difference between WT and mutant cells. A slight reduction was observed in *Vangl2* and *Celsr2* mutant cells; however, rather than a decreased magnitude of displacement, this difference reflected the fact that BB patches remained at the center in some *Vangl2*^{cKO} cells and exhibited an abnormal shape in *Celsr2*$^{-/-}$ cells. These results indicate that, in absence of functional PCP proteins, ependymal cells remain able to cluster their BBs in an off-centered patch and that the molecular machinery required for the displacement per se is not impacted by PCP.

The altered shape of cilia patches observed in some mutants prompted us to analyze further the organization of BB lattices. Contrary to studies of *Xenopus* epidermal cells, which are facilitated by the availability of markers used in immunofluorescence (26–28), mammalian cilia polarity is usually investigated by transmission EM (4, 6, 7, 29, 30), which is hardly compatible with tissue-wide polarity analysis. To circumvent this difficulty, we tested a variety of markers and found that phospho–β-catenin (P-βCat) (31–33), Chibby (29), FGFR1 Oncogene Partner (34), and Clamp (26, 35) localized at the base of cilia, and when combined with γ-tubulin immunostaining, they clearly delineate cilia polarity. The P-βCat signal was adjacent to that of γ-tubulin; at the side opposite to the basal foot, a lateral extension of BBs pointing in the direction of the cilia beats effective stroke (Fig. 3*B*). The double immunostaining allowed the definition of a vector Vcil that represents the polarity of each cilium (Fig. 3 *A* and *B*). As

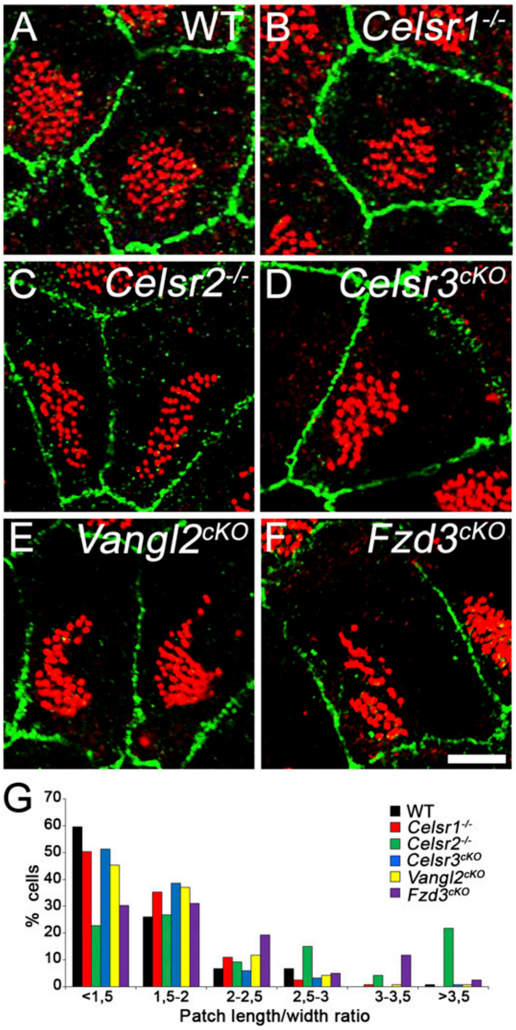

Fig. 2. The clustering and off-centering of BBs are preserved in PCP mutants. (*A–F*) P21 cells from (*A*) WT, (*B*) *Celsr1*$^{-/-}$, (*C*) *Celsr2*$^{-/-}$, (*D*) *Celsr3*^{cKO}, (*E*) *Vangl2*^{cKO}, and (*F*) *Fzd3*^{cKO} stained for ZO1 (green) and γ-tubulin (red). In all genotypes, BBs regroup into off-centered patches that are generally round in WT and *Celsr1*$^{-/-}$ but exhibit irregular shapes in *Celsr2*$^{-/-}$, *Celsr3*^{cKO}, *Vangl2*^{cKO}, and *Fzd3*^{cKO}. Relative distance of displacement calculated as the ratio of the distance between the centers of the apical surface and the patch divided by the distance between the cell center and the membrane: WT: 0.40 ± 0.02, 1,193 cells; *Celsr1*$^{-/-}$: 0.38 ± 0.03, $P = 0.1859$, 1,107 cells; *Celsr2*$^{-/-}$: 0.34 ± 0.01, $P = 0.0007$, 730 cells; *Celsr3*^{cKO}: 0.38 ± 0.02, $P = 0.1764$, 439 cells; *Vangl2*^{cKO}: 0.35 ± 0.02, $P = 0.0086$, 1,013 cells; *Fzd3*^{cKO}: 0.34 ± 0.03, $P = 0.1559$, 557 cells. Five animals per genotype, four animals for *Fzd3*^{cKO}, and three animals for *Celsr3*^{cKO}. (*G*) Distribution of cells according to the patch length/width ratio. Contingency table test compared with WT: *Celsr1*$^{-/-}$: $P = 0.268$; *Celsr2*$^{-/-}$: $P < 0.0001$; *Celsr3*^{cKO}: $P = 0.1831$; *Vangl2*^{cKO}: $P = 0.1411$; *Fzd3*^{cKO}: $P < 0.0001$. One hundred twenty cells for each genotype; three animals per genotype. (Scale bar: 5 μm.)

previously described (6), BBs were randomly oriented in P4 WT cells, resulting in high circular SD (CSD) of Vcil vectors. At P21, patches exhibited a stereotypic organization: BBs were aligned in parallel rows that contained comparable numbers of regularly spaced BBs. Furthermore, BBs were uniformly oriented as reflected in the low CSDs (Fig. 3 *C*, *C*′, and *J*). We defined the resultant of individual Vcils as the vector of patch orientation VpatchO, an indicator of rotational polarity and cilia beat direction in a given cell (Fig. 3*C*′ and Fig. S5 *C* and *D*). In *Celsr1*- and *Fzd3*-deficient cells, the stereotypic arrangement of cilia (spacing and number of cilia per row) was relatively preserved (Fig. 3 *D*, *D*′, *H*, and *H*′). In contrast, it was markedly impaired in *Celsr2*$^{-/-}$, *Celsr3*^{cKO}, and *Vangl2*^{cKO} mutants. In *Celsr2*$^{-/-}$ cells, whereas cilia orientation was normal, the number and spacing of BBs varied from one row to the other, thus affecting the overall shape of the patch (Fig. 3 *E* and *E*′ and quantified in Fig. 3*I*). In *Celsr3*^{cKO} and *Vangl2*^{cKO} cells, the distance between BBs was unaffected, but cilia failed to adopt a uniform alignment and formed oblique, perpendicular, or even opposing rows (Fig. 3 *F*′, red arrows; *G*′, red arrows; and *I*). This abnormal organization resulted in higher CSDs than in WT cells (Fig. 3*J*). Remarkably, a global orientation of Vcil and thus, VpatchO could be readily defined in cells with a CSD below 40°, which represents 99.7% of cells in WT, 91.2% of cells in *Celsr1*$^{-/-}$, 99.6% of cells in *Celsr2*$^{-/-}$, 84.2% of cells in *Celsr3*^{cKO}, 86% of cells in *Vangl2*^{cKO}, and 96.9% of cells in *Fzd3*^{cKO} (Fig. 3*J*).

Altogether, these results show that *Celsr2*, *Celsr3*, *Fzd3*, and *Vangl2* control the intrinsic organization of ciliary patches at the single-cell level.

Loss of Tissue-Wide Polarity in *Celsr1*, *Fzd3*, and *Vangl2* Mutants. As mentioned above, in mutant cells, BB patches are decentered and display a preferential orientation (VpatchO). However, does PCP coordinate these processes at the tissue level? To address this question, we defined VpatchDs as vectors from the center of the apical surface to the center of the patch. VpatchDs reflect the direction of patch displacement and are indicators of translational polarity (Fig. 4 *A*–*B*′ and Figs. S5*E* and S6 *A*–*D*′). We used VpatchD and VpatchO to compare cilia patches in large fields of the ependyma.

In WT, the direction of patch displacement was similar in neighboring cells in a given region of the LW, which was shown by similar VpatchDs (Fig. 4*A*′ and Fig. S1 *L*–*P*). Likewise, the orientation of patches was uniform, with VpatchOs systematically pointing to similar directions (Fig. 4*A*′ and Fig. S1 *L*–*O*′ and *Q*). In contrast, in *Celsr1*$^{-/-}$ and *Vangl2*^{cKO} mutants, we observed a less uniform displacement and orientation of patches: VpatchDs of adjacent cells sometimes pointed to or opposed each other (Fig. 4*B*′ and Fig. S6 *C* and *C*′), and VpatchOs pointed in divergent directions (Fig. 4*E*′ and Fig. S6 *G* and *G*′). We quantified this by measuring angles between individual VpatchDs, VpatchOs, and their respective means. Both VpatchD and VpatchO angles displayed broader circular distributions in *Celsr1*$^{-/-}$ and *Vangl2*^{cKO} mutants compared with WT, confirming the dispersal of patch displacement (Fig. 4*C*) and orientation (Fig. 4*F*). A larger distribution of VpatchDs was also seen in *Fzd3*^{cKO} tissue (Fig. 4*C* and Fig. S6 *D* and *D*′). Analysis of *Celsr2*$^{-/-}$ and *Celsr3*^{cKO} mutants did not reveal any striking difference in the coordination of patch displacement or orientation (Fig. 4 *C* and *F* and Fig. S6 *A*–*B*′ and *E*–*F*′). These results show that *Celsr1*, *Vangl2*, and to a lesser extent, *Fzd3* are required for the intercellular coordination of patch displacement and orientation.

In individual WT cells, the direction of VpatchD coincides with that of VpatchO (Fig. 4 *G* and *G*′ and Fig. S5). This correlation was lost in *Celsr1* mutants, where we frequently observed cells with perfectly organized cilia patches but a VpatchO pointing in a different direction relative to VpatchD (Fig. 4 *H* and *H*′). A similar phenotype was observed in *Vangl2*^{cKO} and *Fzd3*^{cKO} but not *Celsr2*$^{-/-}$ or *Celsr3*^{cKO} cells (Fig. S6 *I*–*L*′). We quantified this by measuring angles between VpatchD and VpatchO. Whereas these angles were below 45° in WT, *Celsr2*$^{-/-}$, and *Celsr3*^{cKO}, larger angles, up to 180°, were observed in *Celsr1*, *Fzd3*, and *Vangl2* mutants (Fig. 4*I*), indicating an uncoupling between the direction of patch displacement and patch orientation in absence of *Celsr1*, *Fzd3*, and *Vangl2*.

Cytoskeletal Changes Associated with Planar Polarization of the Ependyma. Our results suggest a dual role for PCP in cilia organization at the single-cell and tissue levels. Given the importance of the cytoskeleton in ciliogenesis and cilia polarity (15, 26, 27, 30, 36, 37), we examined the actin and microtubule (MT) networks during the transition from RG to ependymal cells (Fig. 5).

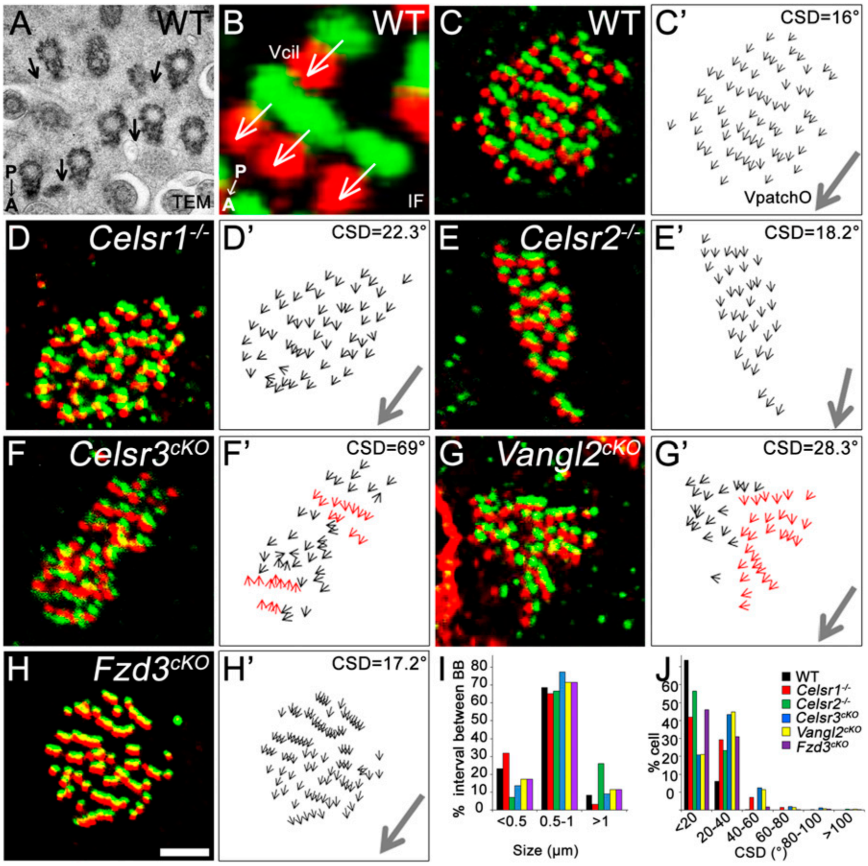

Fig. 3. *Celsr2*, *Celsr3*, *Fzd3*, and *Vangl2* organize cilia in individual cells. (*A*) Transmission EM (TEM) micrograph of a P21 WT cell at the level of basal bodies. The orientation of each cilium is outlined by the basal foot (arrows). (*B*–*H*) Cilia patch of (*B* and *C*) WT, (*D*) *Celsr1*$^{-/-}$, (*E*) *Celsr2*$^{-/-}$, (*F*) *Celsr3*^{cKO}, (*G*) *Vangl2*^{cKO}, and (*H*) *Fzd3*^{cKO} stained for γ-tubulin (red) and P-βCat (green). (*B*) The vector from the P-βCat to the γ-tubulin signals was defined as Vcil. (*C′*–*H′*) Vcils of the patches shown in *C*–*H*. (*C′*–*E′* and *H′*) In WT, *Celsr1*$^{-/-}$, *Celsr2*$^{-/-}$, and *Fzd3*^{cKO}, individual Vcils (black arrows) point in similar directions, illustrating the coordination of cilia orientation. (*F′* and *G′*) In *Celsr3*^{cKO} and *Vangl2*^{cKO}, red Vcils highlight rows of BBs with oblique or opposite orientations compared with the rest of the patch. We defined VpatchO (gray arrows) as the mean direction of Vcils. (*I*) Distribution of BBs according to their spacing. Contingency table test compared with WT: *Celsr1*$^{-/-}$: $P = 0.1488$; *Celsr2*$^{-/-}$: $P < 0.0001$; *Celsr3*^{cKO}: $P = 0.2528$; *Vangl2*^{cKO}: $P = 0.5461$; *Fzd3*^{cKO}: $P = 0.1481$; 30 cells per genotype from three animals. (*J*) Distribution of cells according to Vcil CSD. Contingency table test compared with WT: *Celsr1*$^{-/-}$: $P < 0.0001$; *Celsr2*$^{-/-}$: $P = 0.0055$; *Celsr3*^{cKO}: $P < 0.0001$; *Vangl2*^{cKO}: $P < 0.0001$; *Fzd3*^{cKO}: $P < 0.0001$; $n = 341$ cells for WT; $n = 385$ for *Celsr1*$^{-/-}$; $n = 244$ for *Celsr2*$^{-/-}$; $n = 316$ for *Celsr3*^{cKO}; $n = 406$ for *Vangl2*^{cKO}. Three mice per genotype. A, anterior; IF, immunofluorescence; P, posterior. (Scale bar: *A*, 1 μm; *B*, 0.5 μm; *C*–*H*, 3 μm.)

In RG cells, F-actin (stained with phalloidin) was associated with cell junctions (Fig. 5*A*). α-Tubulin immunostaining disclosed a seedbed of MT centered at the base of the primary cilium (Fig. 5*F*), and immunostaining for the plus-end MT protein EB3 suggested that MT extended from the centrosome to the apical cell cortex (Fig. 5*I*). In maturing cells, phalloidin, α-tubulin, and EB3 staining revealed a concomitant development of actin and MT networks between BBs (Fig. 5 *B*, *G*, and *J*). In fully mature cells, two sets of MTs were observed. The first set juxtaposed the actin meshwork and underlined the patch of BBs (Fig. 5 *H* and *K*), and the second set extended between the patch and the cell cortex (Fig. 5 *H* and *K*, white arrows). The MT anchoring point at the cell cortex localized similarly in neighboring cells (Fig. 5 *L* and *L′* and quantified in Fig. 5*O*). Thus, the cytoskeleton of ependymal cells has a cellular (actin and MT networks of the patch) as well as a tissular (MT anchoring point) component. We analyzed the two components in *Celsr2* and *Celsr1* mutants, which have defects in single-cell and tissue-wide polarity, respectively. We assessed the anchoring of MT to the cell cortex by drawing vectors joining the center of the cell and that of the EB3 membrane-associated sector (Fig. 5 *L*–*N′*). In *Celsr2*$^{-/-}$, the angular deviation of those vectors from the mean was comprised between −45° and +45°, illustrating the tissular coordination of the anchoring point of cortical MTs (Fig. 5 *N*, *N′*, and *O*), but the intrapatch cytoskeleton was disorganized. Actin filaments were stretched and more widely spread compared with WT (compare Fig. 5*C* with Fig. 5*E* and compare Fig. 5*C′* with Fig. 5*E′*). In sharp contrast, whereas no abnormality was seen in the intracellular cytoskeleton (Fig. 5 *D* and *D′*), the MT anchoring point was less coordinated between cells in *Celsr1*$^{-/-}$ mutant, which was reflected by the wide distribution of angular deviations (Fig. 5 *M*, *M′*, and *O*). Altogether, these results show that multiple cytoskeletal rearrangements occur during the polarization of the ependymal layer and that *Celsr2* and *Celsr1* mutations are associated with defects in the cellular and tissular organizations of the cytoskeleton.

Continuum of Tissue-Wide Polarity from RG to Ependymal Cells. In ependymal and tracheal cells, orientation of BBs correlates with a polarized partition of PCP proteins (5, 6). However, the relationship between the position of BBs and the partitioning of PCP proteins during the transition from RG to ependymal cells is unclear. To investigate this relationship, we examined the distribution of Celsr1 and Vangl2 proteins during development. At E12.5, E14.5, and E16.5, Celsr1 and Vangl2 were evenly distributed at the cell contour (Fig. S7 *A*–*C′* and *G*–*I′*). A bias in Celsr1

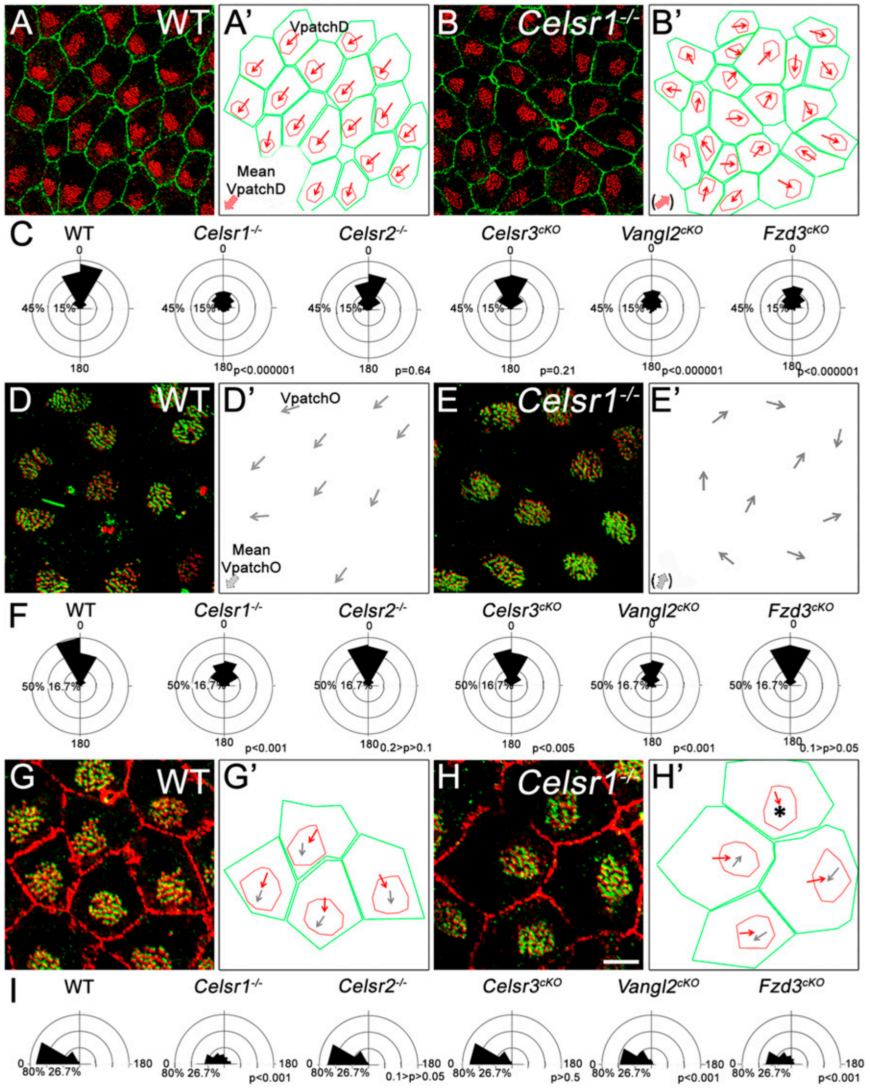

Fig. 4. Tissue-wide polarity is lost in *Celsr1*, *Fzd3*, and *Vangl2* mutants. (*A* and *B*) LW from (*A*) WT and (*B*) $Celsr1^{-/-}$ at P21 stained for ZO1 (green) and γ-tubulin (red). (*A′* and *B′*) Outlines of cell (green) and patch (red) contours. Red arrows, VpatchDs; thick red arrows, mean VpatchD. (*C*) Circular dispersion of VpatchDs around the mean in WT (1,193 cells), $Celsr^{-/-}$ (1,107 cells), $Celsr2^{-/-}$ (730 cells), $Celsr3^{cKO}$ (425 cells), $Vangl2^{cKO}$ (1,013 cells), and $Fzd3^{cKO}$ (557 cells); three animals in $Celsr3^{cKO}$, four animals in $Fzd3^{cKO}$, and five animals in other genotypes. Kolmogorov–Smirnov test compared with WT: $Celsr1^{-/-} = 4.184809$, $P < 0.000001$; $Celsr2^{-/-} = 0.742048$, $P = 0.640565$; $Celsr3^{cKO} = 1.060287$, $P = 0.210884$; $Vangl2^{cKO} = 3.930813$, $P < 0.000001$; $Fzd3^{cKO} = 2.884657$, $P < 0.000001$. (*D* and *E*) LW of (*D*) WT and (*E*) $Celsr1^{-/-}$ P21 mice stained for P-βCat (green) and γ-tubulin (red). (*D′* and *E′*) VpatchOs of cells shown in *D*–*E*. Large gray arrows, mean VpatchO; thin gray arrows, individual VpatchOs. (*F*) Circular dispersion of VpatchOs around the mean in WT (340 cells), $Celsr1^{-/-}$ (351 cells), $Celsr2^{-/-}$ (243 cells), $Celsr3^{cKO}$ (266 cells), $Vangl2^{cKO}$ (350 cells), and $Fzd3^{cKO}$ (557 cells); three animals per genotype. Watson U^2 compared with WT: $Celsr1^{-/-} = 2.644$, $P < 0.001$; $Celsr2^{-/-} = 0.138$, $0.2 > P > 0.1$; $Celsr3^{cKO} = 0.333$, $P < 0.005$; $Vangl2^{cKO} = 2.645$, $P < 0.001$; $Fzd3^{cKO} = 0.164$, $0.1 > P > 0.05$. (*G* and *H*) LW from (*G*) WT and (*H*) $Celsr1^{-/-}$ P21 mice stained for ZO1 (cell contour; red), γ-tubulin (BB; red dots), and P-βCat (green). (*G′* and *H′*) Comparison of VpatchD (red arrows) and VpatchO (gray arrows) in cells shown in *G* and *H*. *A cell in which VpatchO could not be defined. (*I*) Distribution of angles between VpatchD and VpatchO in WT (340 cells), $Celsr1^{-/-}$ (351 cells), $Celsr2^{-/-}$ (243 cells), $Celsr3^{cKO}$ (266 cells), $Vangl2^{cKO}$ (350 cells), and $Fzd3^{cko}$ (205 cells); three animals per genotype. Watson U^2 compared with WT: $Celsr1^{-/-} = 3.294$, $P < 0.001$; $Celsr2^{-/-} = 0.183$, $0.1 > P > 0.05$; $Celsr3^{cKO} = 0.046$, $P > 0.5$; $Vangl2^{cKO} = 0.725$, $P < 0.001$; $Fzd3^{cKO} = 2,186$, $P < 0.001$. (Scale bar: *A*, 15 μm; *D*–*H*, 5 μm.)

and Vangl2 distribution appeared perinatally in some cells (Fig. 6*A* and Fig. S7 *D* and *D′*). It was gradually enhanced and extended to the whole tissue during ependymal maturation (Fig. 6*B*). The asymmetric distribution of Celsr1 and Vangl2 was firmly established in fully mature cells and coordinated across the tissue (Fig. 6*C* and Fig. S7 *E* and *E′*). The polarized distribution of Vangl2 was preserved in $Celsr2^{-/-}$ and $Celsr3^{cKO}$ mutants (Fig. 6 *E* and *F*). In $Celsr1^{-/-}$, despite the accumulation of Vangl2 in specific sectors of the cell membrane (single-cell polarity), the zigzag pattern characteristic of the mature ependyma was not detectable, indicating defective tissular coordination of polarity (Fig. 6 *C* and *D*). Reciprocally, the distribution of Celsr1 was disturbed on inactivation of *Vangl2* (Fig. S7 *F* and *F′*). We analyzed the distribution of Vangl2 with respect to the position of BBs. In WT, Vangl2 localized opposite to the BB of the primary cilium in RG (Fig. 6 *G* and *G′*) and opposite to BB patches in mature ependymal cells (Fig. 6 *I* and *I′*). The inverse correlation between Vangl2 localization and the position of cilia was preserved in $Celsr1^{-/-}$ individual cells. Therefore, like the positioning of the primary cilium, the localization of Vangl2 was uncoordinated between adjacent RG cells (Fig. 6 *H* and *H′*) along with the positioning of multicilia patches in mature ependymal cells (Fig. 6 *J* and *J′*).

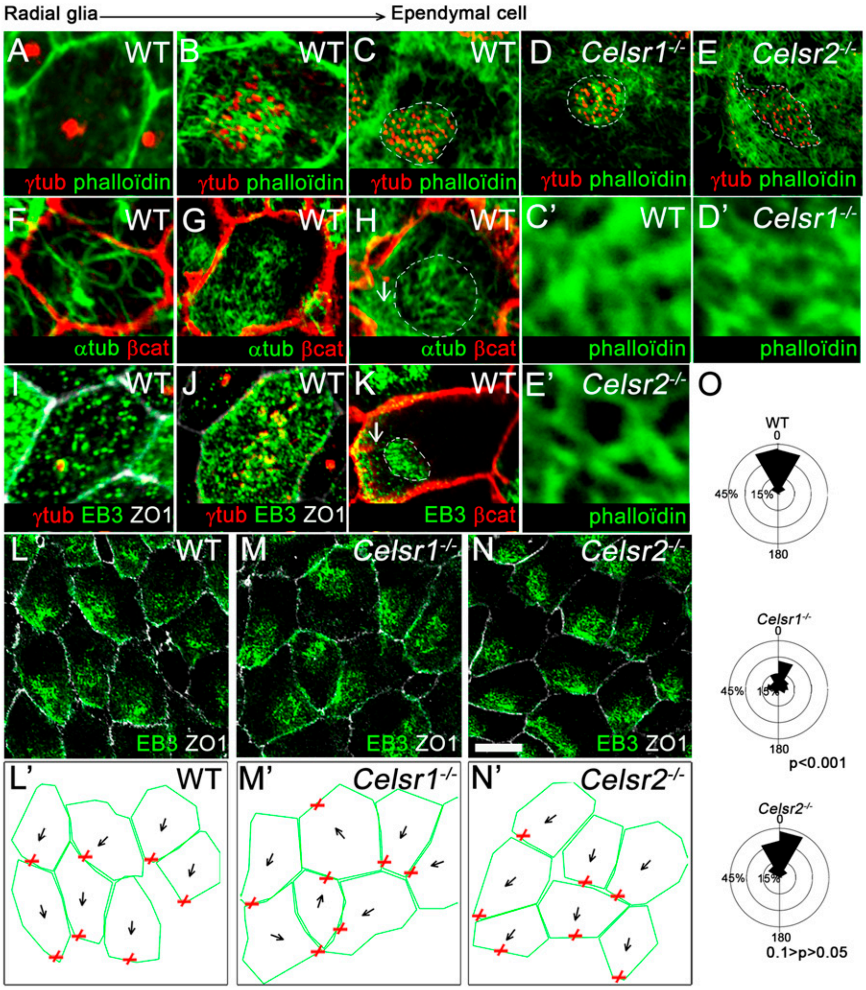

Fig. 5. Cytoskeletal changes associated with ependymal maturation. (*A*–*E*) Cells from (*A*–*C*) WT, (*D*) *Celsr1*$^{-/-}$, and (*E*) *Celsr2*$^{-/-}$ stained with phalloidin (green) and γ-tubulin (red). (*A*) In RG cells (P1), actin is restricted to the membrane. (*B*) In maturing ependymal cells (P5), an actin meshwork arises between BBs. (*C*) In mature ependymal cells (P21), BBs are ensheathed in actin meshwork. (*C*′) High magnification of the meshwork of actin. (*D* and *D*′) A similar meshwork is observed in *Celsr1*$^{-/-}$, whereas (*E* and *E*′) *Celsr2*$^{-/-}$ cells exhibit a loose actin meshwork. (*F*–*K*) WT cells stained for (*F*–*H*) α-tubulin (green) and β-catenin (red), (*I* and *J*) EB3 (green), γ-tubulin (red), and ZO1 (white), or (*K*) EB3 (green) and β-catenin (red). (*F* and *I*) In RG cells, an MT network extends from the primary cilium to the periphery. (*G* and *J*) In maturing cells, a meshwork of MT is seen between sparse BBs. (*H* and *K*) In mature ependymal cells, a first set of MT is observed underneath BBs (dashed outline), and a second set is observed between the patch and the cell cortex (white arrows). (*L*–*N*) P21 LW from (*L*) WT, (*M*) *Celsr1*$^{-/-}$, and (*N*) *Celsr2*$^{-/-}$ stained with ZO1 (white) and EB3 (green). (*L*′–*N*′) Outline of the fields shown in *L*–*N*. Red × depicts the center of EB3 immunostaining and represents the anchoring point of MT at the cell cortex. Black arrows represent vectors between the cell center and the anchoring point. (*O*) Circular dispersion of vectors around the mean. Note the broad distribution of vectors in *Celsr1*$^{-/-}$ (n = 373 cells in WT, n = 401 cells in *Celsr1*$^{-/-}$, n = 302 cells in *Celsr2*$^{-/-}$; three animals for each genotype; Watson U^2 compared with WT: *Celsr1*$^{-/-}$ = 3.271, $P < 0.001$; *Celsr2*$^{-/-}$ = 0.195, $0.1 > P > 0.05$). (Scale bar: *A*, *F*, and *I*, 3 μm; *B*, *G*, *H*, *J*, and *K*, 6 μm; *C*′–*E*′, 1 μm; *L*–*N*, 15 μm.)

MT play a key role in partition of PCP proteins in the fly wing epithelium and the vertebrate trachea (36, 38), and we show that a network of MT was extending toward the cell membrane at the time of polarization of PCP proteins. To test whether MT could be instrumental in distributing those proteins, we injected Nocadazole in brain ventricles of newborn animals and analyzed the localization of Celsr1 and Vangl2 2 d postinjection (Fig. S8). In injected animals (n = 5), most of Celsr1 and Vangl2 staining was seen in the cytoplasm, and although the signal was sometimes associated with the membrane, its distribution was not coordinated between cells (Fig. S8 *B*–*C*′′′). Thus, disassembling of MT dramatically impairs the trafficking and partition of PCP proteins.

Loss of Tissue Polarity Impairs the CSF Flow. Normal CSF circulation depends on the coordinated beating of ependymal cilia and rotational polarity (4, 5). To probe the impact of defective tissue-wide polarity, we analyzed fluid flow by recording the movement of fluorescent beads released at the dorsal anterior aspect of freshly dissected lateral walls from WT and *Celsr1*$^{-/-}$ mice (Fig. 7 *A* and *B*). In the WT tissue, beads moved along two main streams, which are directed anteriorly and merge ventrally (Fig. 7*C*) (n = 5 animals). This stereotypic pattern of bead displacement was not detected in *Celsr1*$^{-/-}$ preparations. We occasionally observed posteriorly directed or swirling movements, indicating the absence of a clearly directed flow. Furthermore, randomly distributed accumulations suggested that beads were confronted locally to opposite flows (Fig. 7*D*, arrowheads) (n = 4 animals). In line with this finding, *Celsr1*$^{-/-}$ mice developed hydrocephalus, likely because of abnormal CSF circulation in vivo (Fig. 7 *E* and *F*).

Discussion

The polarization of the ependyma is a protracted and multifaceted process that starts in RG cells, the precursors of ependymal

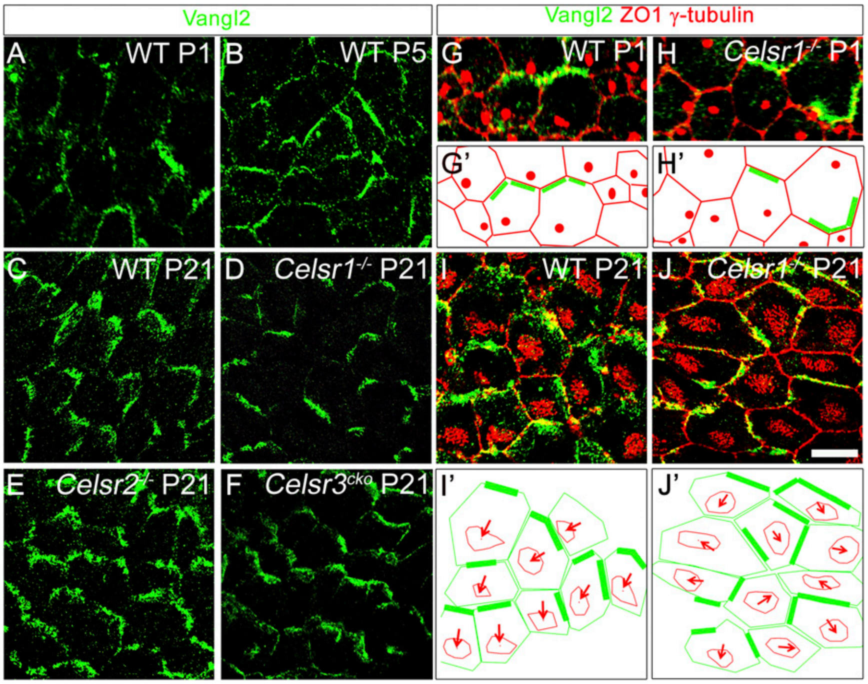

Fig. 6. BBs are located at the opposite side relative to Vangl2. (*A*–*F*) LW from WT at (*A*) P1, (*B*) P5, and (*C*) P21 and (*D*) *Celsr1*$^{-/-}$, (*E*) *Celsr2*$^{-/-}$, and (*F*) *Celsr3*^{cKO} at P21 stained for Vangl2 (green). Vangl2 is gradually enriched at the posterior area of the cell contour. In WT, *Celsr2*$^{-/-}$, and *Celsr3*^{cKO} at P21, polarity is evidenced by the zigzag-like pattern. (*D*) In *Celsr1*$^{-/-}$, Vangl2 is also confined to some subdomains, but the distribution is not coordinated at the tissue level. (*G*–*J*) LW from WT at (*G*) P1 or (*I*) P21 and *Celsr1*$^{-/-}$ at (*H*) P1 or (*J*) P21 stained for ZO1 (red), γ-tubulin (red), and Vangl2 (green). (*G*′ and *H*′) Outline of cell contours (red) and BB (red dot) showing the accumulation of Vangl2 protein (green bars) relative to the primary cilium localization. Vangl2 is systematically facing the primary cilium. (*I*′ and *J*′) Outline of cell contours (green) and patches (red) showing the direction of patch displacement (VpatchD; red arrows) relatively to Vangl2 localization (green bars). BB patches localize opposite to Vangl2. (Scale bar: *A*, *B*, *G*, and *H*, 10 μm; *C*–*F* and *I*–*J*, 15 μm.)

cells. Whereas inactivation of *Celsr2*, *Celsr3*, *Fzd3*, and *Vangl2* perturbs the organization of ependymal multicilia at the single-cell level, inactivation of *Celsr1*, *Fzd3*, and *Vangl2* perturbs the tissue-wide polarity of monocilia in RG and multicilia in ependymal cells. Our observations provide a hint at the control of planar polarity in radial progenitors and suggest a link between this polarity and that of ependymal cells.

Mutant mice lacking the primary cilium have impaired positioning of multicilia (7). We found that mislocalization of the primary cilium correlates with an uncoordinated partition of PCP proteins and abnormal displacement and orientation of multicilia. Importantly, the relationship between the position of the primary cilium in RG cells, the asymmetric accumulation of PCP proteins in differentiating cells, and the positioning of muticilia in ependymal cells is preserved at the single-cell level, suggesting that the concerted and uniform positioning of the primary cilium is a critical event that helps single cells to adjust their polarity to that of their neighbors without affecting their intrinsic ability to become individually polarized. Off-centering of the primary cilium precedes the asymmetric distribution of PCP proteins. MTs grow from the primary cilium toward the cell cortex, and their disruption perturbs the partition of PCP proteins. Thus, as in the fly wing epithelium (38) and mouse tracheal cells, MT may lay the track for a preferential trafficking of PCP proteins in differentiating ependymal cells. The off-center positioning of the primary cilium could provide a bias that breaks symmetry and facilitates the polarized distribution of PCP proteins. Interactions among these proteins are important to stabilize PCP complexes at specific domains of the cell membrane, which was evidenced by the Vangl2/Fzd3 mutual exclusion described in multiple epithelia (2, 10, 11, 13). In ependymal cells, Vangl2 accumulates at a specific side, and Fzd3 would localize in the juxtaposed cell membrane of the adjacent cell. This polarized distribution may, in turn, instruct cells about the location where the cilia patch should be anchored, thereby coordinating organization of motile cilia (Fig. 8).

During differentiation of RG into ependymal cells, BBs of multicilia are initially widely scattered at the apical domain. In addition to their orientation, the ultimate organization of BBs includes their alignment in rows with regular spacing. The implication of PCP proteins in ependymal rotational polarity is well-documented, and MTs play critical roles in this process (5, 6, 15, 27, 30). We show here that PCP signaling is involved in additional aspects of the patch geometry. Indeed, Celsr2 loss of function perturbs the intrapatch actin cytoskeleton and the stereotypic lattice-like arrangement of BBs.

Altogether, our data show that the intrinsic organization of cilia patches in individual cells on the one hand and the coordination of patch orientation and displacement in the whole tissue on the other hand depend on dual PCP signals that may be orchestrated by different *Celsr*s. The former requires *Celsr2* and *Celsr3*, whereas the latter depends on *Celsr1* (Fig. 8). Hence, like their *Drosophila* ortholog *flamingo*/*starry night* (39), Celsr proteins may serve as sorting factors that coordinate the assembly and/or stabilization of specific protein complexes, thereby inducing different pathways and cellular responses. In this context, it is worth noting that Dvl1, Dvl2, and Dvl3, which regulate cilia polarity in the frog epidermis (26), have different expression patterns in ventricular zones (16) as well as specific subcellular distributions in tracheal and ependymal cells, with Dvl2 located at the base of cilia and Dvl1 and Dvl3 located at the cell cortex (15, 36). Consistent with this particular expression, Dvl2 is implicated in rotational but not translational polarity (15). Dvl1 and Dvl3 are expressed in ventricular zones (16) and distributed at cell junctions, making them ideal candidates to convey tissue polarity signals downstream of Celsr1 in RG and ependymal cells.

A role for fluid flow in orientation of motile multicilia (rotational polarity) was reported in *Xenopus* epidermal multiciliated cells (40) and murine ependymal cells (6). Our data, together with published data (7), indicate that the direction of displacement of the primary and motile cilia is indifferent to anatomical axes but always coincides with the functional axis, suggesting that, in addition to PCP signaling, CSF flow could be instrumental in translational polarity. A previous study suggested that fluid flow alone is not sufficient to induce translational planar polarity in primary cultures of ependymal cells (15). Additional investigations are needed to experimentally manipulate the flow and assess its role in translational polarity of primary and motile cilia.

In rodents, the function of ependymal cilia is important for CSF circulation and neurogenesis (41, 42), and the pattern of cilia beats depends on their orientation and spacing (3, 4, 43–45). Our results show that the positioning of cilia across the whole ependymal layer is also critical for their function. The fact that all these process are regulated by PCP highlights its importance in brain homeostasis. Investigations of PCP signaling are, therefore, essential for a better understanding of diseases, such as hydrocephalus and other ciliopathies.

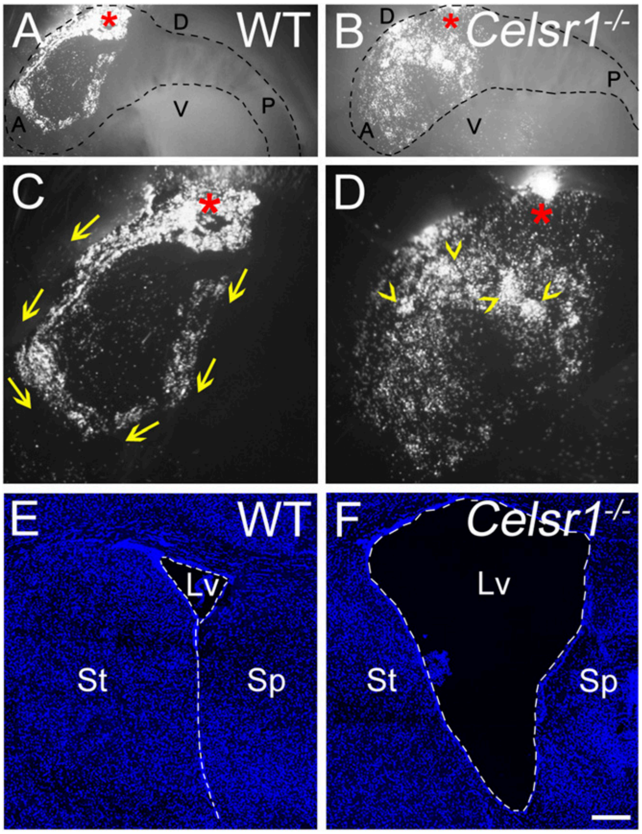

Fig. 7. Fluid flow is impaired in absence of Celsr1. (*A* and *B*) Superposition of bright-field and fluorescent images illustrating the displacement of beads at the surface of the (*A*) WT and (*B*) *Celsr1*$^{-/-}$ samples. Dashed lines delineate LW. *Site of bead release. *C* and *D* are high-magnification views of *A* and *B*. (*C*) In WT, beads move along two anteriorly directed paths (arrows). (*D*) In *Celsr1*$^{-/-}$ sample, lines of migration are absent, with patchy and random accumulation of beads (arrowheads). (*E* and *F*) DAPI-stained P21 brain coronal sections at the level of lateral ventricles (Lvs; dashed line) in (*E*) WT and (*F*) *Celsr1*$^{-/-}$, showing the enlargement of Lv in *Celsr1*$^{-/-}$ mice. A, anterior; D, dorsal; P, posterior; Sp, septum; St, striatum; V, ventral. (Scale bar: *A* and *B*, 800 μm; *C*–*F*, 500 μm.)

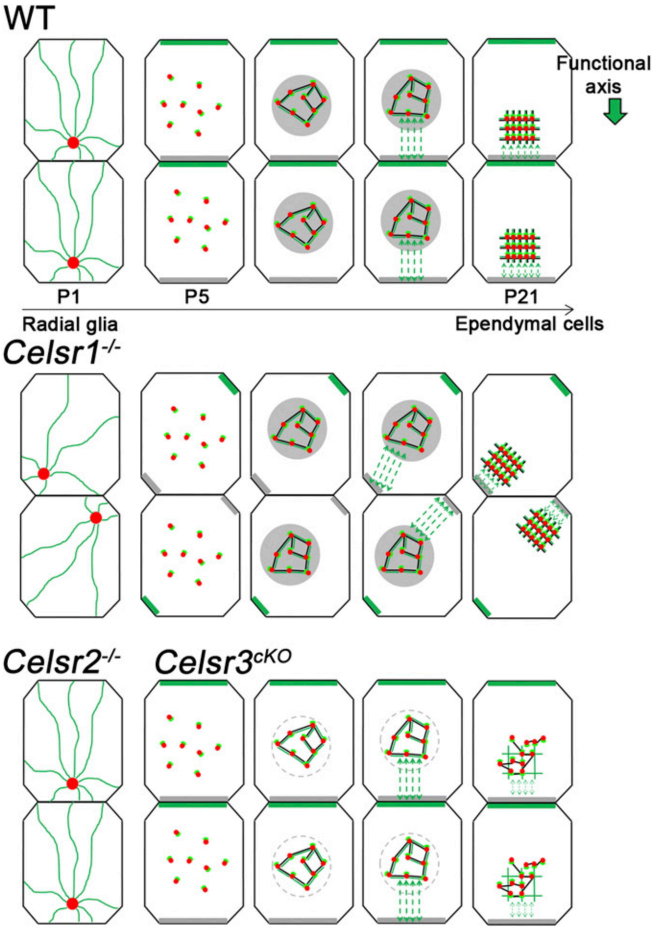

Fig. 8. Working model for the role of PCP in ependymal polarity. Apical surface during transition from RG (P1) to ependymal cells (P21). In WT, the BB of the primary cilium (red dot) is off-centered. An MT network (green) extending from the centrosome to the cortex generates a biased distribution of PCP proteins (gray bars, putatively Fzd3; green bars, Vangl2). At P5, BBs of multicilia (dots) appear widespread and randomly oriented. Concomitant to BB clustering, actin (black) and MT (green) meshworks appear underneath the surface (gray area). MTs (green dashed arrows) connect patches and the cell cortex. In *Celsr1*$^{-/-}$, the primary cilium localization and PCP protein distribution are impaired. The patch–cortex MT interactions occur, but the altered distribution of proteins lead to abnormal positioning and orientation of the BB patch. In contrast, actin and MT networks located in the patch area are unaffected, which results in a normal organization of the BB array. In *Celsr2*$^{-/-}$and *Celsr3*^{cKO}, the primary cilium is correctly positioned, and it correlates with a normal partition of PCP proteins. Patch–cortex MT interactions are preserved, and patches are correctly positioned and orientated. At the level of individual BB patches, the intrapatch cytoskeleton and the shape of BB array are altered.

Materials and Methods

Mutant Mice. All animal procedures were carried out in accordance with European guidelines and approved by the Animal Ethics Committee of the University of Louvain. Mutant mice *Celsr1*$^{-/-}$, *Celsr3*$^{-/-}$, and *Fzd3*$^{-/-}$ were described previously (5, 22, 46, 47). To generate the *Celsr2*$^{-/-}$ allele, two loxP sites flanking the neomycin cassette were inserted in intron 15, and a third site was inserted in intron 28 (Fig. S1). After removal of the neomycin cassette, we obtained *Celsr2 f* mice (*Celsr2*$^{f/f}$), which were crossed to PGK-Cre to delete exons 16–28 and produce *Celsr2*$^{-/-}$. To generate conditional *Celsr3* and *Vangl2* KO mice (*Celsr3*^{cKO} and *Vangl2*^{cKO}), *FoxG1-Cre;Celsr3*$^{+/-}$ and *FoxG-Cre;Vangl2*$^{+/-}$ males were crossed with *Celsr3*$^{f/f}$ (48) and *Vangl2* $^{f/f}$ (24) females, respectively. *Fzd3*^{cKO} mice were described elsewhere (23).

Statistical Analyses. For classical statistics, two-tailed Student *t* test was calculated using Graphpad Prism 5. Contingency table (Excel) tests were used to compare each mutant genotype with the WT. For circular statistics, WT and the different genotypes were compared using the Watson U^2 test (Oriana software) or Kolmogorov–Smirnov test (Matlab). A minimum of three animals were analyzed for each genotype.

RT-PCR. Total RNA was extracted using the RNeasy Midi Kit (75142; Qiagen) according to the manufacturer's instructions. RNA integrity was assessed by ethidium bromide staining of formaldehyde gels. RNA was converted into single-stranded cDNA using the Impro-II Reverse Transcription System (A3800; Promega) with random primers (0.5 μg/mL) in 20 μL 1× ImPro-II buffer containing 6 mM $MgCl_2$, 0.5 mM each dNTP, and 20 U recombinant RNasin ribonuclease inhibitor. For subsequent PCR amplification, we used the following primers: Celsr2 forward primer 5′-CCAGAACGCTTTCTCTCACC-3′ [Geninfo identifier (gi): 24475635, nucleotides 3412–3431; exon 2], Celsr2 reverse primer 5′-CCACAAAGTCGTGCTTCTCA-3′ (gi: 24475635, nucleotides 4233–4252; exon 4), p73 forward primer 5′-CAGCTCCTACAGAGGCCGAG-3′ (gi: 41945505; nucleotides 1167–1186), and p73 reverse primer 5′-CTCGATGCAGTTTGGACACC-3′ (gi: 41945505, nucleotides 1489–1508).

Nocodazole Injections. Two microliters 25% (vol/vol) DMSO in PBS or 2 mM Nocodazole solution (dissolved in 25% DMSO in PBS; Sigma) was injected into the lateral ventricle of P0 mice. Coordinates for injections were defined as previously described (49). Animals were killed and processed for immunostaining 2 d after injection.

Immunostaining on LW Whole Mounts. Immunostainings on LW whole-mount preparations were performed as described (7). Briefly, freshly dissected LWs were fixed for 15 min in 4% paraformaldehyde and 0.1% Triton X-100. They were washed three times in PBS, incubated for 1 h in PBS and 3% BSA blocking solution, incubated overnight with primary antibodies diluted in PBS, 0.1% Triton X-100, and 3% BSA, and incubated 1 h with secondary antibodies. LWs were dissected further and mounted with Mowiol. Primary antibodies are mouse IgG1 anti–γ-tubulin (1:500; Abcam), mouse IgG anti-ZO1 (1:400; Invitrogen), rabbit anti-ZO1 (1:400; Invitrogen), mouse IgG antiacetyl–α-tubulin (1:1,000; Sigma) rabbit antiphospho–β-catenin (1:800; Cell Signaling), mouse IgG2a anti-Chibby (1:500; Santa Cruz), mouse IgG2b anti-FGFR1OP (1:2,000; Abnova), rabbit anti-Clamp (1:2,000; gift from Gerard Dougherty, National Institutes of Health, Bethesda), rabbit anti–α-tubulin (1:200; Abcam), rat anti-EB3 (1:100; Abcam), rabbit anti-Vangl2 (1:250; gift from Mireille Montcouquiol, Neurocenter Magendie, Bordeaux, France), phalloidin-A488 (1:50; Invitrogen), and guinea pig anti-Celsr1 (1:800). Secondary antibodies are Alexa Fluor 488 goat anti-rabbit (1:800; Invitrogen), Alexa Fluor 647 goat anti-rabbit (1:800; Invitrogen), Alexa Fluor 568 F(ab′)2 fragment of goat anti-mouse IgG (1:800; Invitrogen), Alexa Fluor 488 F(ab′)2 fragment of goat anti-mouse IgG (1:800; Invitrogen), Alexa Fluor 488 goat anti-guinea pig (1:800; Invitrogen), Alexa Fluor 488 donkey anti-rat (1:800; Invitrogen), and Alexa Fluor 488 goat anti-guinea pig (1:800; Invitrogen).

EM. LWs were dissected and incubated overnight in fixative (2.5% glutaraldehyde in 0.1 M cacodylate buffer, pH 7.5). Blocks were rinsed, postfixed in 1% osmium, and embedded in epoxy resin. Thin sections were stained with uranyl acetate and lead citrate and observed with a ZEISS EM 912 microscope.

Image Acquisition and Data Quantification. LW whole-mount preparations were analyzed on a laser-scanning confocal microscope (Olympus Fluoview FV1000) using a 60× oil Uplsapo objective with 1.35 N.A. Images were acquired using the Fluoview software (Olympus). Five nonoverlapping fields (50 × 50 μm for P1 and 100 × 100 μm for P21) were acquired for each sample. The distance between BBs was measured using the FV10-ASW 3.1 software (Olympus). All of the other analyses and quantifications were performed using homemade software Biotool1 (github.com/pol51/biotool1). For analysis of γ-tubulin and ZO1 immunostainings, the contours of ependymal cells and BBs patches were manually traced. The software was used to calculate (*i*) the geometric center of these contours, (*ii*) the relative surface of the BB patch as a percentage of the apical surface of the cell, and (*iii*) the normalized BB displacement relative to the cell center (calculated as the distance between the cell center and the primary cilium BB or the patch center divided by the distance from the cell center to the membrane). For the two latter parameters, the mean per animal was calculated from raw data and plotted as a histogram using Excel. To analyze the coordination of patch displacement, VpatchD was defined from the center of the cell to the center of the patch, and the deviation of individual vectors relative to the mean vector of the field was calculated. A similar strategy was used to evaluate the coordination of the primary cilium displacement. In that case, a vector was drawn between the center of the cell and the primary cilium BB. Cells in which the BB is superposed to the center were not considered.

For analysis of ciliary patches using P-βCat and γ-tubulin double immunostaining, dots corresponding to both signals were manually defined for each cilium. A unit vector connecting the two dots was defined by the software. These vectors were used to calculate the CSD of each patch. The distribution of cells in the different bins of CSD was done in Excel. The coordination of patch orientation was analyzed from the same manual acquisition. Only cells with CSD below 40° were considered to define VpatchO (mean Vcil). The deviation of individual VpatchOs relative to the mean VpatchO was calculated to evaluate the tissular coordination of the patch orientation.

To analyze the intracellular coordination of VpatchD and VpatchO, cells, patches, and Vcils were defined after manual tracing on ZO1, P-βCat, and γ-tubulin triple immunostaining. Angles between individual VpatchDs and VpatchOs were calculated.

The output of Biotool1 is a list of angles that were plotted in Oriana software (Kovach Computing Services) to obtain the graphical representation of their distribution in 30° bins and perform circular statistical analysis. In all circular representations, the percentage of cells is represented as the radius of wedge.

Analysis of Fluid Flow. Analysis of the fluid flow generated by ependymal cells was performed as described (7) with minor modifications. In brief, freshly dissected lateral walls from WT or mutant animals were immobilized in Petri dishes containing Leibovitz media at 37 °C. Hand-pulled glass capillaries were used to release a solution containing 10% GFP-fluorescent microbeads (2-μm diameter; ref. 09847; Biovalley) and 5% glycerol in water at the anterior dorsal part of the lateral wall. Bead movements were recorded using a Leica DFC 420 camera (1 frame/s) mounted on a Leica TL stereomicroscope. Several rounds of beads release were performed for each ventricle during a maximum of 15 min. During the course of the experiment, beads progressively dropped along the flow pathway. At the end of recordings, nondeposed beads remaining in the medium were flushed away, and deposits of beads on the roof of lateral ventricle were photographed.

ACKNOWLEDGMENTS. We thank Jean Hébert for the Foxg1-Cre line, Gerard Dougherty for Clamp antibodies, and Isabelle Lambermont, Esther Paitre, and Rachid El Kaddouri for technical assistance. This work was supported by Fonds de la Recherche Scientifique Medicale Grant 3.4550.11, Belgian National Fund for Scientific Research Grant T0002.13, Actions de Recherches Concertées Grant ARC-10/15-026, a Fondation médicale Reine Elisabeth grant, a Fondation JED-Belgique grant, a Desordres Inflamatoires dans les Affections Neurologiques grant, a Welbio grant from the Région wallonne, and Inter-University Poles of Attraction Grant PAI P7/20. F.T. is a senior research associate of the Belgian National Fund for Scientific Research.

1. Marshall WF, Kintner C (2008) Cilia orientation and the fluid mechanics of development. *Curr Opin Cell Biol* 20(1):48–52.
2. Wallingford JB (2012) Planar cell polarity and the developmental control of cell behavior in vertebrate embryos. *Annu Rev Cell Dev Biol* 28:627–653.
3. Ibañez-Tallon I, et al. (2004) Dysfunction of axonemal dynein heavy chain Mdnah5 inhibits ependymal flow and reveals a novel mechanism for hydrocephalus formation. *Hum Mol Genet* 13(18):2133–2141.
4. Lechtreck KF, Delmotte P, Robinson ML, Sanderson MJ, Witman GB (2008) Mutations in Hydin impair ciliary motility in mice. *J Cell Biol* 180(3):633–643.
5. Tissir F, et al. (2010) Lack of cadherins Celsr2 and Celsr3 impairs ependymal ciliogenesis, leading to fatal hydrocephalus. *Nat Neurosci* 13(6):700–707.
6. Guirao B, et al. (2010) Coupling between hydrodynamic forces and planar cell polarity orients mammalian motile cilia. *Nat Cell Biol* 12(4):341–350.
7. Mirzadeh Z, Han YG, Soriano-Navarro M, García-Verdugo JM, Alvarez-Buylla A (2010) Cilia organize ependymal planar polarity. *J Neurosci* 30(7):2600–2610.
8. Merkle FT, Tramontin AD, García-Verdugo JM, Alvarez-Buylla A (2004) Radial glia give rise to adult neural stem cells in the subventricular zone. *Proc Natl Acad Sci USA* 101(50):17528–17532.
9. Adler PN (2012) The frizzled/stan pathway and planar cell polarity in the Drosophila wing. *Curr Top Dev Biol* 101:1–31.
10. Goodrich LV, Strutt D (2011) Principles of planar polarity in animal development. *Development* 138(10):1877–1892.
11. Gray RS, Roszko I, Solnica-Krezel L (2011) Planar cell polarity: Coordinating morphogenetic cell behaviors with embryonic polarity. *Dev Cell* 21(1):120–133.
12. Struhl G, Casal J, Lawrence PA (2012) Dissecting the molecular bridges that mediate the function of Frizzled in planar cell polarity. *Development* 139(19):3665–3674.

13. Wang Y, Nathans J (2007) Tissue/planar cell polarity in vertebrates: New insights and new questions. *Development* 134(4):647–658.
14. Tissir F, Goffinet AM (2013) Shaping the nervous system: Role of the core planar cell polarity genes. *Nat Rev Neurosci* 14(8):525–535.
15. Hirota Y, et al. (2010) Planar polarity of multiciliated ependymal cells involves the anterior migration of basal bodies regulated by non-muscle myosin II. *Development* 137(18):3037–3046.
16. Tissir F, Goffinet AM (2006) Expression of planar cell polarity genes during development of the mouse CNS. *Eur J Neurosci* 23(3):597–607.
17. Formstone CJ, Little PF (2001) The flamingo-related mouse Celsr family (Celsr1-3) genes exhibit distinct patterns of expression during embryonic development. *Mech Dev* 109(1):91–94.
18. Hadjantonakis AK, et al. (1997) Celsr1, a neural-specific gene encoding an unusual seven-pass transmembrane receptor, maps to mouse chromosome 15 and human chromosome 22qter. *Genomics* 45(1):97–104.
19. Shima Y, et al. (2002) Differential expression of the seven-pass transmembrane cadherin genes Celsr1-3 and distribution of the Celsr2 protein during mouse development. *Dev Dyn* 223(3):321–332.
20. Tissir F, Goffinet AM (2010) Planar cell polarity signaling in neural development. *Curr Opin Neurobiol* 20(5):572–577.
21. Ravni A, Qu Y, Goffinet AM, Tissir F (2009) Planar cell polarity cadherin Celsr1 regulates skin hair patterning in the mouse. *J Invest Dermatol* 129(10):2507–2509.
22. Tissir F, Bar I, Jossin Y, De Backer O, Goffinet AM (2005) Protocadherin Celsr3 is crucial in axonal tract development. *Nat Neurosci* 8(4):451–457.
23. Chai G, et al. (2014) Celsr3 is required in motor neurons to steer their axons in the hindlimb. *Nat Neurosci*, in press.
24. Song H, et al. (2010) Planar cell polarity breaks bilateral symmetry by controlling ciliary positioning. *Nature* 466(7304):378–382.
25. Hébert JM, McConnell SK (2000) Targeting of cre to the Foxg1 (BF-1) locus mediates loxP recombination in the telencephalon and other developing head structures. *Dev Biol* 222(2):296–306.
26. Park TJ, Mitchell BJ, Abitua PB, Kintner C, Wallingford JB (2008) Dishevelled controls apical docking and planar polarization of basal bodies in ciliated epithelial cells. *Nat Genet* 40(7):871–879.
27. Werner ME, et al. (2011) Actin and microtubules drive differential aspects of planar cell polarity in multiciliated cells. *J Cell Biol* 195(1):19–26.
28. Yasunaga T, Itoh K, Sokol SY (2011) Regulation of basal body and ciliary functions by Diversin. *Mech Dev* 128(7-10):376–386.
29. Voronina VA, et al. (2009) Inactivation of Chibby affects function of motile airway cilia. *J Cell Biol* 185(2):225–233.
30. Kunimoto K, et al. (2012) Coordinated ciliary beating requires Odf2-mediated polarization of basal bodies via basal feet. *Cell* 148(1-2):189–200.
31. Chilov D, et al. (2011) Phosphorylated β-catenin localizes to centrosomes of neuronal progenitors and is required for cell polarity and neurogenesis in developing midbrain. *Dev Biol* 357(1):259–268.
32. Hadjihannas MV, Brückner M, Behrens J (2010) Conductin/axin2 and Wnt signalling regulates centrosome cohesion. *EMBO Rep* 11(4):317–324.
33. Corbit KC, et al. (2008) Kif3a constrains beta-catenin-dependent Wnt signalling through dual ciliary and non-ciliary mechanisms. *Nat Cell Biol* 10(1):70–76.
34. Lee JY, Stearns T (2013) FOP is a centriolar satellite protein involved in ciliogenesis. *PLoS ONE* 8(3):e58589.
35. Dougherty GW, et al. (2005) CLAMP, a novel microtubule-associated protein with EB-type calponin homology. *Cell Motil Cytoskeleton* 62(3):141–156.
36. Vladar EK, Bayly RD, Sangoram AM, Scott MP, Axelrod JD (2012) Microtubules enable the planar cell polarity of airway cilia. *Curr Biol* 22(23):2203–2212.
37. Lemullois M, Boisvieux-Ulrich E, Laine MC, Chailley B, Sandoz D (1988) Development and functions of the cytoskeleton during ciliogenesis in metazoa. *Biol Cell* 63(2): 195–208.
38. Shimada Y, Yonemura S, Ohkura H, Strutt D, Uemura T (2006) Polarized transport of Frizzled along the planar microtubule arrays in Drosophila wing epithelium. *Dev Cell* 10(2):209–222.
39. Chen WS, et al. (2008) Asymmetric homotypic interactions of the atypical cadherin flamingo mediate intercellular polarity signaling. *Cell* 133(6):1093–1105.
40. Mitchell B, Jacobs R, Li J, Chien S, Kintner C (2007) A positive feedback mechanism governs the polarity and motion of motile cilia. *Nature* 447(7140):97–101.
41. Lehtinen MK, et al. (2011) The cerebrospinal fluid provides a proliferative niche for neural progenitor cells. *Neuron* 69(5):893–905.
42. Town T, et al. (2008) The stumpy gene is required for mammalian ciliogenesis. *Proc Natl Acad Sci USA* 105(8):2853–2858.
43. Banizs B, et al. (2005) Dysfunctional cilia lead to altered ependyma and choroid plexus function, and result in the formation of hydrocephalus. *Development* 132(23): 5329–5339.
44. Eley L, Yates LM, Goodship JA (2005) Cilia and disease. *Curr Opin Genet Dev* 15(3): 308–314.
45. Marshall WF (2008) The cell biological basis of ciliary disease. *J Cell Biol* 180(1):17–21.
46. Tissir F, et al. (2009) DeltaNp73 regulates neuronal survival in vivo. *Proc Natl Acad Sci USA* 106(39):16871–16876.
47. Wang Y, Thekdi N, Smallwood PM, Macke JP, Nathans J (2002) Frizzled-3 is required for the development of major fiber tracts in the rostral CNS. *J Neurosci* 22(19): 8563–8573.
48. Zhou L, et al. (2008) Early forebrain wiring: Genetic dissection using conditional Celsr3 mutant mice. *Science* 320(5878):946–949.
49. Boutin C, Diestel S, Desoeuvre A, Tiveron MC, Cremer H (2008) Efficient in vivo electroporation of the postnatal rodent forebrain. *PLoS One* 3(4):e1883.